Research Article | Vol. 29, No. 1 / 4 January 2021 / Optics Express 170
Optics EXPRESS

Transient transmission of THz metamaterial antennas by impact ionization in a silicon substrate

MATIAS BEJIDE,[1] YEJUN LI,[1,2] NIKOLAS STAVRIAS,[3] BRITTA REDLICH,[3] TAKUO TANAKA,[4,5] VU DINH LAM,[6] NGUYEN THANH TUNG,[6,7] AND EWALD JANSSENS[1,8]

[1]*Quantum Solid-State Physics, Department of Physics and Astronomy, KU Leuven, Leuven, Belgium*
[2]*Department of Physics and Electronics, Central South University, Changsha, China*
[3]*FELIX Laboratory, Institute for Molecules and Materials, Radboud University, Nijmegen, The Netherlands*
[4]*Metamaterials Laboratory, RIKEN Cluster for Pioneering Research, Saitama, Japan*
[5]*Innovative Photon Manipulation Research Team, RIKEN Center for Advanced Photonics, Saitama, Japan*
[6]*Institute of Materials Science and Graduate University of Science and Technology, Vietnam Academy of Science and Technology, Vietnam*
[7]*tungnt@ims.vast.ac.vn*
[8]*ewald.janssens@kuleuven.be*

Abstract: The picosecond dynamics of excited charge carriers in the silicon substrate of THz metamaterial antennas was studied at different wavelengths. Time-resolved THz pump-THz probe spectroscopy was performed with light from a tunable free electron laser in the 9.3–16.7 THz frequency range using fluences of 2–12 J/m^2. Depending on the excitation wavelength with respect to the resonance center, transient transmission increase, decrease, or a combination of both was observed. The transient transmission changes can be explained by local electric field enhancement, which induces impact ionization in the silicon substrate, increasing the local number of charge carriers by several orders of magnitude, and their subsequent diffusion and recombination. The studied metamaterials can be integrated with common semiconductor devices and can potentially be used in sensing applications and THz energy harvesting.

1. Introduction

The electromagnetic properties of metamaterials (MM) depend on the size and periodic arrangement of the components [1–3]. The building blocks of terahertz (THz) MMs, operating in the 0.5–15 THz range, have typical sizes of a few to hundreds of micrometres. In this size range photolithography is a mature fabrication technology. By changing the size and shape of the components, their environment, and the proximity of the neighbouring components; the resonance frequency, bandwidth and the resonance type can be tuned [4–6]. For example, dipole antennas interact strongly with the electric field, while split rings resonate with magnetic fields [7–9].

The THz range, with frequencies in between high frequency electronics (GHz, radio waves) and photonics (from infrared to near UV), is still relatively unexplored. The development of THz radiation sources has greatly advanced the last decades due to optical rectification and optically pumped sources [10–12], while short high-power laser pulses with a large tunable range are still only achievable through vacuum electronics, e.g. free electron lasers. THz frequencies are particularly well suited for research of MMs and THz MM technology, where absorbers, detectors, and modulators have been developed in the last decades [13–15]. Bridging the THz gap may bring great advances to different areas, ranging from basic research in physics and astronomy to medical imaging, telecommunication, single electron control in nanostructures, and

#405555 https://doi.org/10.1364/OE.405555
Journal © 2021 Received 17 Aug 2020; revised 4 Dec 2020; accepted 8 Dec 2020; published 22 Dec 2020

Optics EXPRESS

even the construction sector [13,16]. In particular, THz MMs could be used in the field of energy harvesting since objects above 50 K radiate in the THz range and THz radiation surrounds us in great quantities and in the field of telecommunication because their frequencies allow for the transmission of high-density data streams [3,14,17–20].

Many of the applications listed above are based on nonlinear effects induced by field enhancement (FE) in a semiconducting substrate or inter-antenna nonlinear materials. The FE results from the confinement of the incident electromagnetic fields by the MMs structures. Knowledge about the dynamical processes induced by the FE are important for the design and construction of MMs with improved tunability of their ultrafast properties [3,14,17,21]. In particular, it was shown that THz FE can induce strong charge carrier multiplication in semiconducting materials such as GaAs and silicon [18,19,22,23], which is relevant for photovoltaics, luminescent emitters, and photon detectors. THz spectroscopy is a powerful technique with high potential to study the effect of FE induced nonlinearities on the optical properties of THz MMs [18,24], but has so far only been limited to broadband excitation and short timescales (few ps only). Knowledge about the FE effects in MM is important to avoid high energy electron-induced melting and damage caused by electromigration [25].

Not only the excitation dynamics but also the subsequent carrier relaxation processes, taking place on time scales ranging from less than a picosecond (e.g., electron-electron scattering) to several nanoseconds (bulk electron-hole recombination), are not fully understood. THz pump-THz probe transient transmission spectroscopy, carried out in a broad spectral range around the resonance frequency, can be instrumental in this respect. The development of evermore powerful and faster THz coherent sources, e.g. free electron lasers (FELs), enables the study of the relaxation phenomena and transient effects in nonlinear MMs in a broad spectral range with high temporal resolution [10]. Because of the low availability of THz sources, the potential of THz pump/probe spectroscopy has so far not been fully exploited.

In this work, we study cut-wire (CW) MMs consisting of micrometer sized antennas arranged in a rectangular lattice on top of a boron doped Si substrate. The picosecond (ps) dynamic of a MM is, for the first time, probed by THz pump/THz probe spectroscopy at different wavelengths across the broad transmission gap of the MMs. In combination with electromagnetic simulations, those experiments provide insight in the underlying causes of the transient transmission.

2. Experimental and computational methodology

The transient transmission of the samples was investigated with THz three beam pump-probe spectroscopy (TPPS). Those experiments were carried out at the Free Electron Lasers for Infrared eXperiments (FELIX) laboratory, Nijmegen, the Netherlands [26]. FELIX is continuously tunable in the 3–100 μm spectral range, of which the 18–38 μm range was used for the current experiments. The output of the free electron laser consists of 8 μs long macropulses with a repetition frequency of 10 Hz. Each macropulse consists of a train of micropulses that have a duration of 5–10 ps, corresponding to a spectral width of ~0.5% in the 18–38 μm range (the micropulses are transform limited), with a repetition frequency of 25 MHz. The experiments are performed with a single micropulse, which has a fluence in the range of 2–12 J/m^2 delivered in 8 ps [26]. It was shown that a fluence of about 20 J/m^2, which is above the maximal fluence used in the current study, can generate ripples in a silicon surface [27].

The three laser pulses (pump, probe, and reference) originate from the same micropulse. As illustrated in Fig. 1, a first beam splitter splits off 90% of the pulse energy creating the pump beam. The remaining 10% is split into two identical pulses, the probe and the reference, which are separated in time by half of the micropulse repetition period (i.e., 20 ns). The pump-probe delay is tunable from –200 to 800 ps. The reference beam is used to balance out pulse-to-pulse fluctuations in the laser power and spatial beam profile, increasing the sensitivity of the measurements. The three beams are focused on the sample using a parabolic mirror with a focal length of 152 mm,

Optics EXPRESS

and a pinhole is used to ensure a good overlap of the three beams. The balanced bolometer converts the relative probe to reference transmission into a voltage. The strong pump pulse excites the CW antennas and a delayed probe pulse monitors the transmission as a function of the pump-probe delay time. A negative (positive) probe transmission, relative to the reference transmission, implies that the pump beam has induced a transient decrease (increase) of the sample transmission. This approach implicitly assumes that the initial situation is recovered 20 ns after the pump beam passed through the sample, which is confirmed by the pump-probe dynamics at negative times (if the probe arrives prior to the pump, an unperturbed state of the sample is observed) and by the absence of long term drifts. It is important to mention that there was no damage seen after the experiments upon inspection of the samples with optical microscopy, even at the highest pump fluence.

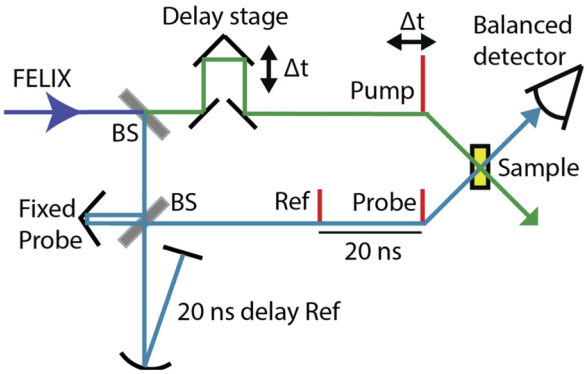

Fig. 1. Schematic view of the pump-probe setup. It shows how the three beams (pump, probe, and reference) are derived from single FELIX pulse, and arranged to reach the sample with desired time delays between each other. BS refers to beam splitter.

The finite integration simulation technique embedded in CST Microwave Studio software was used to compute the dipole resonance [28]. The simulations were performed using the time domain solver for 3.5 ns, with periodic boundaries applied for the $\vec{H}$ and $\vec{E}$ directions, while the propagation direction $\vec{k}$ of the incident electromagnetic wave is kept perpendicular to the sample plane. The modelled silicon substrate was 200 µm thick, which is thick enough to avoid Fabry-Perot interference that tampers with the calculated spectra.

3. Results

Figure 2 shows the transmittance spectrum of the sample, measured with light polarised along the long axis of the antennas and normalised for the transmission of the bare silicon substrate. The linear transmittance spectrum shows a broad transmission gap from 17 to 32 µm with a minimum around 23 µm.

For antennas with negligible neighbour interaction, their dipole resonance wavelengths, which can be approximated as the transmittance minima, follow the antenna resonance equation [5,29–31]:

$$\lambda_{res} = 2 \cdot n_{eff} L \tag{1}$$

with L the length of the antenna and n_{eff} the effective refraction index of the cut wires' environment. n_{eff} depends on the dielectric constant of the substrate ε_{sub} via:

$$n_{\mathrm{eff}} = \sqrt{\varepsilon_{\mathrm{eff}}} = \sqrt{(1 + \varepsilon_{\mathrm{sub}})/2} \tag{2}$$

The resonance frequency thus depends on the dielectric properties of the silicon substrate, which change upon exposure to an intense electric field.

Optics EXPRESS

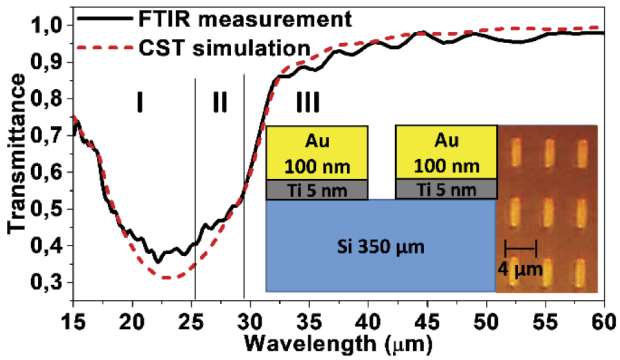

Fig. 2. Experimental (measured using a FTIR setup, Bruker V80) and simulated transmittance spectra of the CW metamaterial sample with 4×1 μm^2 antennas and a 9×5 μm^2 unit cell. The left inset is a schematic cross section (not drawn to scale) of the sample and the right inset is a picture of the sample. Labels I, II, and III denote regions of the spectra with different transient behaviour.

Using Eqs. (1) and (2) to fit FTIR transmission data for samples with antennas sizes ranging from 1 to 15 μm (see Fig. S1 in the Supplement 1), a refractive index for the substrate $n_{sub} = 3.26 \pm 0.09$ is found, close to the reported value of 3.417 for wavelengths around 20 μm [32]. This interpretation ignores the dependence of the wavelength (and the width) of the resonance on the coupling interaction between neighbouring CW antennas, which is small for this geometry according to the simulations. The measured static transmittance spectrum is in outstanding agreement with the spectrum from electromagnetic simulations (red dashed line in Fig. 2).

Figure 3 shows the transient probe transmission of the samples (relative to the reference) in the range from –100 to 650/550 ps at three different wavelengths. The results of experiments performed at additional wavelengths are available as Supplement 1 (Fig. S2). The fast oscillations observed during the first ~15 ps of recorded signal are atributed to the interference of standing waves formed by the incoming and reflected laser pulses, optical autocorrelation, and are ignored in the forthcoming interpretation.

On the blue and center side of the transmittance minimum (e.g. 23 μm excitation wavelength in Fig. 3(a)), a transient transmission increase is observed that lasts several hundreds of picoseconds. At the far red side of the resonance center (Fig. 3(c) at 32 μm), there is a transient transmission decrease. In the spectral range at the red side, but closer to resonance center (Fig. 3(b) at 27.5 μm), the behavior is mixed: there is an initial decrease in the transmission (first ~50 ps) followed by a transmission increase before decaying to the original level. Those three types of transient transmission behavior divide the spectral range in three zones, labelled as I, II, and III in Fig. 2. Also in other samples with different CW dimensions; 2.5×1, 7×1 and 9×1 μm^2; exibiting antenna resonance wavelengths at 17, 35 and 44.5 μm, respectively, similar behavior was observed (see Supplement 1 Fig. S3, S4 and S5).

The observed wavelength dependence in the transmission change can be explained in the following way. The pump pulse induces changes in the system that are reflected in a transient change of the wavelength and intensity of the antenna resonance. As will be explained in more detail in the discussion section, neither a red shift nor a change in the spectral width alone is sufficient to explain the observed dynamics, but a combination of both effects is. It is important to stress that pump and probe laser pulses always have the same wavelength, since they come from the same laser pulse. This means that for each probed wavelength, the pump was different. While the exact wavelength of the pump is not changing the nature of the phenomena taking place

Optics EXPRESS

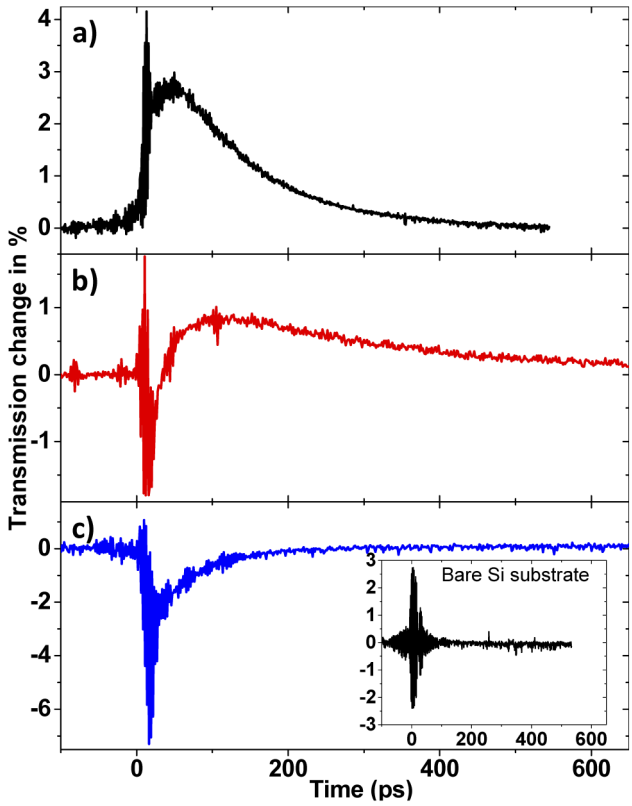

Fig. 3. Transient transmission change following excitation at (a) 23 µm with a 8 J/m^2 fluence, (b) 27.5 µm with a 11 J/m^2 fluence and (c) 32 µm with a 8 J/m^2 fluence. The inset in panel c) presents a TPSS measurement for a bare silicon substrate (32 µm with 5 J/m^2 fluence) without gold antennas. This reference measurement does not show transient transmission dynamics asides from a signal in the first 15 ps that is caused by optical autocorrelation of the probe pulse.

(i.e. impact ionization, explained in the discussion section), the FE changes with the excitation wavelength. The wavelength dependence is related to proximity of the excitation wavelength to the resonance center. To have comparable excitation conditions at different excitation wavelengths, the laser pulse energy was adjusted. Within the used range, the sample response increases monotonically with the laser fluence (see Supplement 1 Fig. S6), allowing for rescaling the measured signal.

4. Discussion

For wavelengths within the broad transmission gap of the MM, the electromagnetic field of the pump pulse causes oscillation of the free electrons of the antenna, which enhances the impinging electric field. This enhanced electric field penetrates the Si substrate and may, if it is strong enough, induce an amplification of the conduction band charge carriers. Such an increase of the charge carriers in silicon, changes its optical and electrical properties (i.e. refractive index and conductivity) and thereby the antenna resonance wavelength and width (see Eqs. (1) and (2)). The change of the optical properties of the system can be detected as a transient transmission.

The FE factor was simulated and used to calculate the value of the penetrating E-field. Considering a 2–12 J/m^2 pump pulse fluence, 0.2 mm^2 spot area, and 8 ps pulse length, the value

Optics EXPRESS

of the incident electric field is of the order of 0.3–0.7 MV/cm. The penetrating enhanced field inside the silicon substrate is in this case of the order of MV/cm.

As illustrated in Fig. 4(a), the FE of a single antenna (with a resonance wavelength of 23 μm) depends on the position in the sample and on the excitation wavelength. As is expected for a dipolar resonance, the FE is higher close to the antenna's edges along the short axis; in particular, close to the corners. The maximum FE is red shifted with respect to the center of the transmittance minimum (vertical dotted line in Fig. 4(a)). This is a well-documented phenomenon. It is analogous to a damped forced harmonic oscillator [33], where the frequency corresponding to the maximal energy dissipation can be related to the minimal transmittance. The frequency corresponding to the maximum oscillation amplitude is lower (red shifted) and can be is related to the maximal FE.

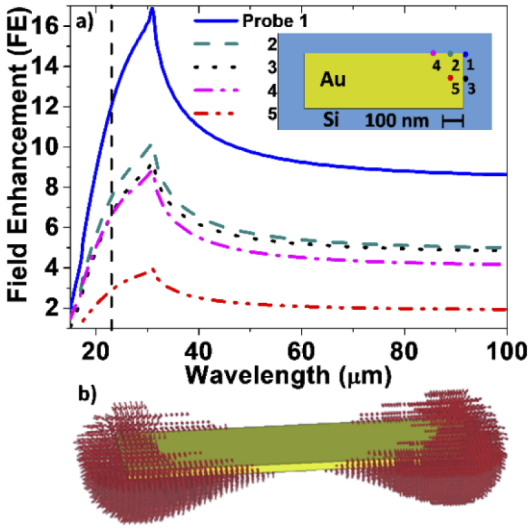

Fig. 4. a) Wavelength dependence of the FE factor at different positions (labelled 1-5). The vertical dashed line indicates the centre of the transmission gap. b) Spatial distribution of the enhanced electric field, the red arrows represent the direction and the magnitude of the electric field in the area where the field is larger than the incident field. The Si substrate, located below the gold antenna, is not shown for clarity.

The enhanced electric field accelerates Si conduction band charge carriers. They may acquire sufficient energy to excite, in a scattering event, a bound valence band charge carrier to the conduction band. This mechanism for carrier multiplication is called impact ionization. It originates from Coulomb interaction between energetic carriers in the conduction and valence band of a semiconductor. [22,23] A cascade of collision events, in which free charge carriers are accelerated by a strong external electric field, increases the number of free carriers by several orders of magnitude. Since the conductivity directly depends on the number of charge carriers in the conduction band, as given by the Drude model [18,22], the increased number of free carriers changes on the electrical and optical response of the semiconductor [18,22,23,34].

The process can be represented by the following equation [23]:

$$e_1 \rightarrow e_1 + e_2 + h_2, \tag{3}$$

with e_1 the conduction band electron being accelerated by the enhanced electric field, and e_2 and h_2 the excited valence band electron and its respective hole. The rate equation for charge carrier

Optics EXPRESS

amplification by impact ionization, ignoring relaxation processes, is:

$$dn(t)/dt = n(t) \int f(E,t) Y_{\mathrm{ii}}(E) dE, \tag{4}$$

with n_0 the initial number of charge carriers, $f(E,t)$ the electron energy distribution, and $Y_{ii}(E)$ the impact ionization rate. Based on the theory developed by Keldysh, with a quadratic dependence of the rate on the energy of the conduction electrons [35], Cartier *et al.* proposed the following expression for the impact ionization rate [36]:

$$Y_{\mathrm{ii}}(E) = \sum_{\mathrm{i}=1}^{3} p^{(\mathrm{i})} \left(\frac{E - E_{\mathrm{th}}^{\mathrm{i}}}{E_{\mathrm{th}}^{\mathrm{i}}} \right)^2 \theta(E(t) - E_{\mathrm{th}}^{\mathrm{i}}), \tag{5}$$

where the sum runs over the possible excitation pathways, namely $i = 1$ the indirect band gap for electrons; $i = 2$ the indirect band gap for holes; and $i = 3$ the direct band gap for electrons. The parameters $p^{(\mathrm{i})}$ are constants, evaluated $3.25{\cdot}10^{10}$, $3.0{\cdot}10^{12}$, and $6.8{\cdot}10^{14}$ s^{-1} for $i = 1$, 2, and 3, respectively [36]. $E(t)$ is the carriers' energy, $E_{\mathrm{th}}^{\mathrm{i}}$ corresponds to different threshold energies for ionization (1.2, 1.85, and 3.45 eV for $i = 1$, 2, 3, respectively) [36], and $\theta(x)$ is the Heaviside function. Given that each enhanced THz semi cycle is equivalent to a very fast electric field pulse, the electron energy distribution can be approximated as a delta function: $f(E,t) = \delta(E - E(t))$ [37]. This simplifies Eq. (4) to:

$$dn(t)/dt = n(t) \sum_{\mathrm{i}=1}^{3} p^{(\mathrm{i})} \left(\frac{E(t) - E_{\mathrm{th}}^{\mathrm{i}}}{E_{\mathrm{th}}^{\mathrm{i}}} \right)^2 \theta(E(t) - E_{\mathrm{th}}^{\mathrm{i}}) \tag{6}$$

To complete the model, the external electric field should be linked to the carriers' energy. This is done by the momentum equation of a Bloch wave in a periodical Coulomb potential including a term for momentum relaxation and the electron dispersion relation [23,38,39].

$$\hbar \frac{dk(t)}{dt} = e\ \varepsilon(\mathrm{t}) - \sum_{\mathrm{i}=1}^{3} k_{\mathrm{th}}^{(\mathrm{i})} p^{(\mathrm{i})} \left(\frac{k(\mathrm{t}) - k_{th}^{i}}{k_{\mathrm{th}}^{\mathrm{i}}} \right)^2 \theta(k(t) - k_{\mathrm{th}}^{\mathrm{i}}) - \frac{k(t)}{\tau}. \tag{7}$$

In this equation $\varepsilon(\mathrm{t})$ represents the enhanced THz pulse, $k(t)$ the carriers' momentum, and τ the momentum decay time. The THz micro pulse is modelled as a sinusoidal wave whose amplitude is modulated by a Gaussian envelope $\varepsilon(\mathrm{t}) = \varepsilon_{\mathrm{FE}} \cos(\omega_0 t) \exp[-1/2 \cdot (t/\sigma)^2]$, where ω_0 is the angular frequency of the THz pulse and σ is related to the pulse duration. For the simulations σ is set to 2 ps and $\varepsilon_{\mathrm{FE}}$ is the enhanced electric field amplitude, i.e., the incident THz field times the FE factor.

The momentum decay time is a complex function that depends on the carriers' drift velocity and the intrinsic carrier-phonon scattering time. We approximate it by [40,41]:

$$\frac{1}{\tau} = \frac{1}{\tau_{eph}} + \frac{e}{m_e \cdot \mu} \tag{8}$$

Here e is the electron charge, μ the electron mobility [41,42], and $\tau_{\mathrm{eph}} = 240$ ps the silicon electron phonon scattering time [40]. This expression represents the energy loss of a conduction band electron due to the influence of an external electric field. This term represents the scattering for charge carriers in silicon.

Equations (6) to (8) describe how the Si substrate is affected by impact ionization. In Fig. 5 the results of solving these equations for several different FE factors and wavelengths are shown. A minimal FE of 3 seems to be needed to cause a significant increase of the number of conduction electrons, at least one order of magnitude. It is consistent with findings in literature where for

Optics EXPRESS

larger bandgap semiconductors, like GaAs and Si; no transmission changes were observed unless a threshold energy, related to a threshold electric field via Eq. (6) and the electron dispersion relation, is surpassed [18,19,22,23]. This is achievable only through FE of the incident electric field given the high intensity required. For narrow band semiconductors (InSb), electron impact ionization could be obtained without the need for field enhancement [39]. For a given FE, longer wavelengths are more efficient to increase the charge carrier concentration due to longer optical cycle and thus more time for the enhanced electric field to interact with the silicon substrate.

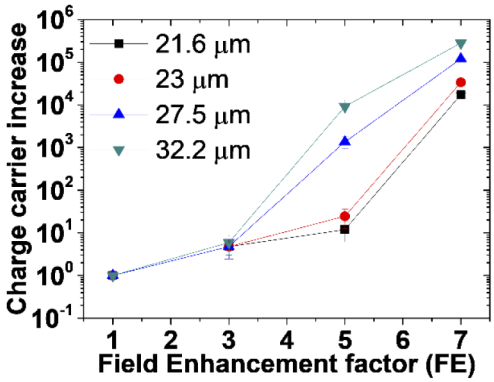

Fig. 5. Relative increase of the conduction band charge carriers as a function of the FE factor for different excitation wavelengths. The values are calculated with a pump pulse fluence of 10 J/m^2 and an initial carrier density of the Si substrate of $5{\cdot}10^{15}$ /cm^3.

The impact ionization model is further used together with the simulation results of the spatial and frequency dependence of the enhanced electric field, to predict the concentration of charge carriers, and thus the conductivity of the silicon, as a function of space and time [41].

So far, the model only describes the first picoseconds when the pump pulse is exciting the antennas. The vast majority of the acquired TPPS data corresponds to later times, during which the enhanced carrier density decreases by electron-hole pair recombination and diffusion. Their density $n(t)$ diminishes by diffusion and recombination by trapping and neutralization. In order to model this, we use a characteristic decay time of $\tau = 200$ ps to account for carrier recombination [24,43] and a density dependent ambipolar carrier diffusion coefficient D [44], to account for volumetric expansion.

$$n(t) = n_0 \frac{\exp(-t/\tau)}{V(t)}, \tag{9}$$

$$V(t) = \sqrt{6D\,t + v_0^2}, \tag{10}$$

with n_0 the carrier density after the impact ionization and $V(t)$ the affected volume, which increases in time due to diffusion [18].

The measured transient signal likely results from a mixture of several types of recombination processes and carrier diffusion, which affect the silicon conductivity in an expanding volume near the antenna's extremes [18,45].

The model provides the local change in conductivity of the substrate at every moment in time for a given value of FE. This information is used as input for the CST simulations, considering an average FE value for the unit cell. Since the antenna resonance depends on the dielectric properties of the substrate, the transient properties of the substrate are reflected in the transmittance spectra of the samples.

The results of these simulations for an excitation wavelength of 27.5 µm and a pump pulse fluence of 11 J/m^2 are shown in Fig. 6. It can be seen that the transmission gap red-shifts and

Optics EXPRESS

broadens during the first few ps, as expected from the results shown in Fig. 3, and thereafter, on a timescale of several tens to a few hundreds of ps, returns to the original situation.

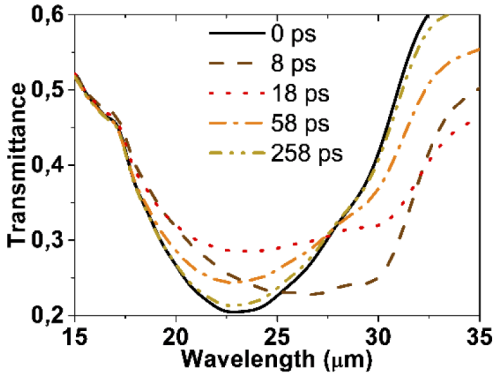

Fig. 6. The shape of the modelled transmittance spectra at different moments after excitation. $t = 0$ ps and $t = 8$ ps correspond to the beginning and the end of the excitation pulse, respectively. The sample geometry corresponds to the one shown in Fig. 2 and the excitation wavelength is 27.5 μm.

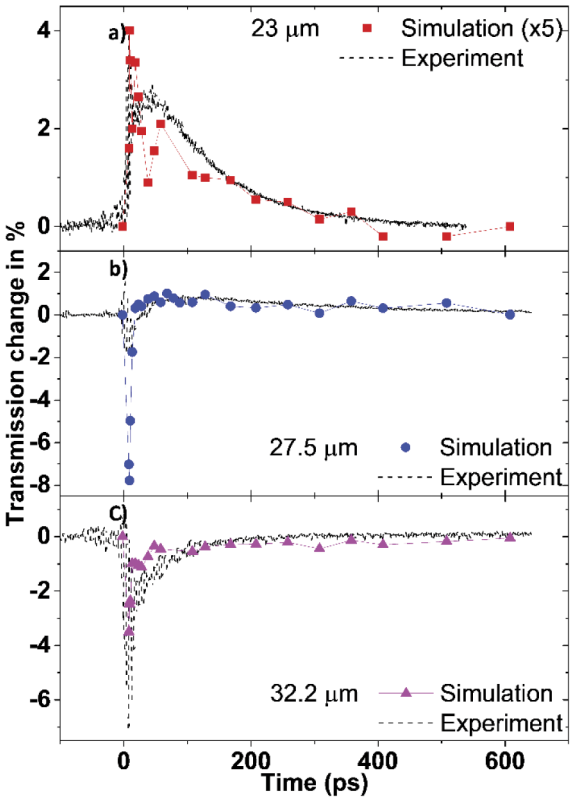

Fig. 7. Simulated transient transmission changes based on the impact ionization model and comparison with the experimental data (same as in Fig. 3) for (a) 23 μm with a 8 J/m^2 fluence, (b) 27.5 μm with a 11 J/m^2 fluence, and (c) 32 μm with a 8 J/m^2 fluence.

Optics EXPRESS

Applying this approach at several wavelengths allows us to qualitatively reproduce the transient transmission changes that were measured at different wavelengths. Figure 7 presents simulations at different wavelengths and pump pulse energies, which correspond to the experimental conditions of the TPPS traces shown in Fig. 3. Comparing the experimental and modelled transmission curves of Fig. 7, one finds a qualitative agreement. The simulations reproduce the observed trends; including the different transient responses at different excitation wavelengths, and the non-instantaneous rise to the maximum transmission change. The good agreement supports the validity of the proposed model for the carrier dynamics. Quantitative differences can be attributed to a rough description of momentum/energy dissipation of the excited charge carriers during the impact ionization; oversimplification of the conductivity changes in the affected silicon volume and the detailed FE spatial distribution; and inaccuracies of the simulations related to the size and shape of the affected volume.

5. Conclusion

We have studied the transient transmission of THz metamaterials with spectral resolution by three-beam pump-probe spectroscopy using an infrared free electron laser. The strong THz field of the pump beam was found to be locally enhanced by the resonance mode of micrometer sized cut-wire antennas. Impact ionization increases the carrier concentration in the silicon substrate by several orders of magnitude. The increase and decay of these high carrier densities results in fast nonlinear changes in the optical properties of the MM. Following picosecond THz excitation, the transmission gap red-shifts and broadens during the first few picoseconds and the sample relaxes to the original situation on a timescale of several tens to a few hundreds of ps. This behavior is qualitatively reproduced and interpreted by the described impact ionization model.

MM on semiconducting substrates have potential to be used in energy harvesting devices at THz frequencies if the materials are further optimized geometrically such that less intense electric fields are required to induce the strong charge carrier increase. Due to their sensitivity to the environment, those MM may also have potential in sensing applications. There are still several unanswered fundamental questions about the excitation and relaxation processes. In future experiments one could explore substrates with different types and levels of doping, as well as different sample temperatures. Future work could also involve different structural designs, which allow for even higher FE factors in order to maximize carrier multiplication.

Funding. Laserlab-Europe (grant 654148 within the European Union's Horizon 2020 research and innovation programme); Fonds Wetenschappelijk Onderzoek (G0E62.18N); National Foundation for Science and Technology Development (FWO.103.2017.01).

Acknowledgment. The authors also thank the Nederlandse Organisatie voor Wetenschappelijk Onderzoek (NWO) for the support of the FELIX Laboratory.

Disclosures. The authors declare no conflicts of interest. EJ and NTT conceived and designed the research; TT, VDL, and NTT prepared the samples; MB, YL, NS, BR, and EJ carried out TTPS and FTIR measurements; MB and YL analysed the experimental data, MB, NTT, and EJ conducted the simulations and calculations; MB, NTT and EJ prepared the manuscript. All authors have edited, reviewed and given approval to the final version of the manuscript.

See Supplement 1 for supporting content.

References

1. W. Cai and V. Shalaev, *Optical Metamaterials: Fundamentals and Applications* (Springer-Verlag, 2010).
2. J. H. Woo, B. Kang, M. Gwon, J. H. Lee, D. W. Kim, W. Jo, D. H. Kim, and J. W. Wu, "Time-Resolved Pump–Probe Measurement of Optical Rotatory Dispersion in Chiral Metamaterial," Adv. Opt. Mater. **5**(15), 1700141 (2017).
3. A. S. Shorokhov, K. I. Okhlopkov, J. Reinhold, C. Helgert, M. R. Shcherbakov, T. Pertsch, and A. A. Fedyanin, "Ultrafast control of third-order optical nonlinearities in fishnet metamaterials," Sci. Rep. **6**(1), 28440 (2016).
4. N. I. Landy, S. Sajuyigbe, J. J. Mock, D. R. Smith, and W. J. Padilla, "Perfect metamaterial absorber," Phys. Rev. Lett. **100**(20), 207402 (2008).
5. F. Neubrech, T. Kolb, R. Lovrincic, G. Fahsold, A. Pucci, J. Aizpurua, T. W. Cornelius, M. E. Toimil-Molares, R. Neumann, and S. Karim, "Resonances of individual metal nanowires in the infrared," Appl. Phys. Lett. **89**(25), 253104 (2006).

Optics EXPRESS

6. W. A. Murray and W. L. Barnes, "Plasmonic materials," Adv. Mater. **19**(22), 3771–3782 (2007).
7. J. B. Pendry, A. J. Holden, D. J. Robbins, and W. J. Stewart, "Magnetism from conductors and enhanced nonlinear phenomena," IEEE Trans. Microwave Theory Technol. **47**(11), 2075–2084 (1999).
8. D. R. Smith, W. J. Padilla, D. C. Vier, S. C. Nemat-Nasser, and S. Schultz, "Composite Medium with Simultaneously Negative Permeability and Permittivity," Phys. Rev. Lett. **84**(18), 4184–4187 (2000).
9. N. T. Tung, Y. P. Lee, and V. D. Lam, "Transmission properties of electromagnetic metamaterials: From split-ring resonator to fishnet structure," Opt. Rev. **16**(6), 578–582 (2009).
10. P. Salén, M. Basini, S. Bonetti, J. Hebling, M. Krasilnikov, A. Y. Nikitin, G. Shamuilov, Z. Tibai, V. Zhaunerchyk, and V. Goryashko, "Matter manipulation with extreme terahertz light: Progress in the enabling THz technology," Phys. Rep. **836-837**, 1–74 (2019).
11. R. A. Lewis, "A review of terahertz sources," J. Phys. D: Appl. Phys. **47**(37), 374001 (2014).
12. G. Gallerano and S. Biedron, "Overview of terahertz radiation sources," *Proc. 2004 FEL Conf.*, 216–221 (2004).
13. C. Sirtori, "Applied physics: Bridge for the terahertz gap," Nature **417**(6885), 132–133 (2002).
14. G. R. Keiser and P. Klarskov, "Terahertz field confinement in nonlinear metamaterials and near-field imaging," Photonics **6**(1), 22 (2019).
15. M. Beruete and I. Jáuregui-López, "Terahertz Sensing Based on Metasurfaces," Adv. Opt. Mater. **8**(3), 1900721 (2020).
16. T. Rybka, M. Ludwig, M. F. Schmalz, V. Knittel, D. Brida, and A. Leitenstorfer, "Sub-cycle optical phase control of nanotunnelling in the single-electron regime," Nat. Photonics **10**(10), 667–670 (2016).
17. N. Kamaraju, A. Rubano, L. Jian, S. Saha, T. Venkatesan, J. Nötzold, R. Kramer Campen, M. Wolf, and T. Kampfrath, "Subcycle control of terahertz waveform polarization using all-optically induced transient metamaterials," Light: Sci. Appl. **3**(2), e155 (2014).
18. C. Lange, T. Maag, M. Hohenleutner, S. Baierl, O. Schubert, E. R. J. Edwards, D. Bougeard, G. Woltersdorf, and R. Huber, "Extremely nonperturbative nonlinearities in GaAs driven by atomically strong terahertz fields in gold metamaterials," Phys. Rev. Lett. **113**(22), 227401 (2014).
19. K. Fan, H. Y. Hwang, M. Liu, A. C. Strikwerda, A. Sternbach, J. Zhang, X. Zhao, X. Zhang, K. A. Nelson, and R. D. Averitt, "Nonlinear terahertz metamaterials via field-enhanced carrier dynamics in GaAs," Phys. Rev. Lett. **110**(21), 217404 (2013).
20. X. Chen, Z. Tian, Y. Lu, Y. Xu, X. Zhang, C. Ouyang, J. Gu, J. Han, and W. Zhang, "Electrically Tunable Perfect Terahertz Absorber Based on a Graphene Salisbury Screen Hybrid Metasurface," Adv. Opt. Mater. **8**(3), 1900660 (2020).
21. H. R. Seren, J. Zhang, G. R. Keiser, S. J. Maddox, X. Zhao, K. Fan, S. R. Bank, X. Zhang, and R. D. Averitt, "Nonlinear terahertz devices utilizing semiconducting plasmonic metamaterials," Light: Sci. Appl. **5**(5), e16078 (2016).
22. A. T. Tarekegne, K. Iwaszczuk, M. Zalkovskij, A. C. Strikwerda, and P. U. Jepsen, "Impact ionization in high resistivity silicon induced by an intense terahertz field enhanced by an antenna array," New J. Phys. **17**(4), 043002 (2015).
23. H. Hirori, K. Shinokita, M. Shirai, S. Tani, Y. Kadoya, and K. Tanaka, "Extraordinary carrier multiplication gated by a picosecond electric field pulse," Nat. Commun. **2**(1), 594–596 (2011).
24. G. Choi, Y. M. Bahk, T. Kang, Y. Lee, B. H. Son, Y. H. Ahn, M. Seo, and D.-S. Kim, "Terahertz Nanoprobing of Semiconductor Surface Dynamics," Nano Lett. **17**(10), 6397–6401 (2017).
25. J. Zhang, X. Zhao, K. Fan, X. Wang, G. F. Zhang, K. Geng, X. Zhang, and R. D. Averitt, "Terahertz radiation-induced sub-cycle field electron emission across a split-gap dipole antenna," Appl. Phys. Lett. **107**(23), 231101 (2015).
26. "Radboud University," https://www.ru.nl/felix/facility-0/measurement-station/pump-probe-station/.
27. A. Irizawa, S. Suga, T. Nagashima, A. Higashiya, M. Hashida, and S. Sakabe, "Laser-induced fine structures on silicon exposed to THz-FEL," Appl. Phys. Lett. **111**(25), 251602 (2017).
28. "Dasault Systemes," https://www.cst.com.
29. E. Cubukcu and F. Capasso, "Optical nanorod antennas as dispersive one-dimensional Fabry-Perot resonators for surface plasmons," Appl. Phys. Lett. **95**(20), 201101 (2009).
30. K. B. Crozier, A. Sundaramurthy, G. S. Kino, and C. F. Quate, "Optical antennas: Resonators for local field enhancement," J. Appl. Phys. **94**(7), 4632–4642 (2003).
31. A. Pucci, F. Neubrech, J. Aizpurua, T. Cornelius, and M. L. de la Chapelle, "Electromagnetic Nanowire Resonances for Field-Enhanced Spectroscopy," in *One-Dimensional Nanostructures*, Z. M. Wang, ed. (Springer-Verlag, 2008), Vol. 3, pp. 175–215.
32. D. Chandler-Horowitz and P. M. Amirtharaj, "High-accuracy, midinfrared (450 cm -1 $\leq\omega\leq$4000 cm -1) refractive index values of silicon," J. Appl. Phys. **97**(12), 123526 (2005).
33. J. Chen, P. Albella, Z. Pirzadeh, P. Alonso-González, F. Huth, S. Bonetti, V. Bonanni, J. Åkerman, J. Nogués, P. Vavassori, A. Dmitriev, J. Aizpurua, and R. Hillenbrand, "Plasmonic nickel nanoantennas," Small **7**(16), 2341–2347 (2011).
34. Y.-G. Jeong, M. J. Paul, S.-H. Kim, K.-J. Yee, D.-S. Kim, and Y.-S. Lee, "Large enhancement of nonlinear terahertz absorption in intrinsic GaAs by plasmonic nano antennas," Appl. Phys. Lett. **103**(17), 171109 (2013).
35. L. V. Keldysh, "Concerning the Theory of Impact Ionization in Semiconductors," Sov. Phys. JETP **21**(6), 1135–1144 (1965).

Optics EXPRESS

36. E. Cartier, M. V. Fischetti, E. A. Eklund, and F. R. McFeely, "Impact ionization in silicon," Appl. Phys. Lett. **62**(25), 3339–3341 (1993).
37. H. Wen, M. Wiczer, and A. M. Lindenberg, "Ultrafast electron cascades in semiconductors driven by intense femtosecond terahertz pulses," Phys. Rev. B **78**(12), 125203 (2008).
38. W. Kuehn, P. Gaal, K. Reimann, M. Woerner, T. Elsaesser, and R. Hey, "Coherent ballistic motion of electrons in a periodic potential," Phys. Rev. Lett. **104**(14), 146602 (2010).
39. M. C. Hoffmann, J. Hebling, H. Y. Hwang, K. Lo Yeh, and K. A. Nelson, "Impact ionization in InSb probed by terahertz pump-terahertz probe spectroscopy," Phys. Rev. B **79**(16), 161201 (2009).
40. T. Sjodin, H. Petek, and H. L. Dai, "Ultrafast carrier dynamics in silicon: A two-color transient reflection grating study on a (111) surface," Phys. Rev. Lett. **81**(25), 5664–5667 (1998).
41. B. Van Zeghbroeck, *Principles of Electronic Devices* (University of Colorado, 2011).
42. S. Basu, B. J. Lee, and Z. M. Zhang, "Infrared Radiative Properties of Heavily Doped Silicon at Room Temperature," J. Heat Transfer **132**(2), 023301 (2010).
43. Y. Yang, Y. Yan, M. Yang, S. Choi, K. Zhu, J. M. Luther, and M. C. Beard, "Low surface recombination velocity in solution-grown $CH_3NH_3PbBr_3$ perovskite single crystal," Nat. Commun. **6**(1), 7961 (2015).
44. J. F. Young and H. M. van Driel, "Ambipolar diffusion of high-density electrons and holes in Ge, Si, and GaAs: Many-body effects," Phys. Rev. B **26**(4), 2147–2158 (1982).
45. A. Richter, S. W. Glunz, F. Werner, J. Schmidt, and A. Cuevas, "Improved quantitative description of Auger recombination in crystalline silicon," Phys. Rev. B **86**(16), 165202 (2012).